

## WMAP OBSERVATIONS OF *Planck* ESZ CLUSTERS

YIN-ZHE MA,<sup>1,2</sup> GARY HINSHAW,<sup>1</sup> DOUGLAS SCOTT,<sup>1</sup>

*Draft version September 24, 2018*

### ABSTRACT

We examine the Sunyaev–Zeldovich (SZ) effect in the 7-yr *Wilkinson Microwave Anisotropy Probe* (*WMAP*) data by cross-correlating it with the *Planck* Early-release Sunyaev–Zeldovich catalog. Our analysis proceeds in two parts. We first perform a stacking analysis in which the filtered *WMAP* data are averaged at the locations of the 175 *Planck* clusters. We then perform a regression analysis to compare the mean amplitude of the SZ signal,  $Y_{500}$ , in the *WMAP* data to the corresponding amplitude in the *Planck* data. The aggregate *Planck* clusters are detected in the 7-yr *WMAP* data with a signal-to-noise ratio of 16.3. In the regression analysis we find that the SZ amplitude measurements agree to better than 25%:  $a = 1.23 \pm 0.18$  for the fit  $Y_{500}^{\text{wmap}} = aY_{500}^{\text{planck}}$ .

*Subject headings:* cosmic microwave background — cosmology: observations — galaxies: clusters: general — large scale structure of universe

### 1. INTRODUCTION

Clusters of galaxies are important objects for studying cosmology and large-scale structure formation. In hot clusters, around 12% of their mass is in the form of a hot, ionized intra-cluster medium (ICM, McCarthy et al. 2007). The ICM can be studied using direct X-ray imaging and/or the Sunyaev-Zeldovich effect (SZ, Sunyaev & Zeldovich 1972, 1980). Observations of the latter have grown tremendously in recent years thanks to an array of powerful new instruments (Birkinshaw & Gull 1978; Birkinshaw 1999; Carlstrom et al. 2002).

The thermal SZ effect is a secondary anisotropy in the cosmic microwave background (CMB) radiation, caused by CMB photons scattering off free electrons in the hot ICM through the inverse Compton effect. The effect boosts the photon’s energy and thus distorts the CMB spectrum in the direction of a cluster, causing a temperature decrement on the low frequency side of the CMB peak (specifically,  $\nu < 217$  GHz), and an increment at high frequencies.

The SZ effect is especially powerful for studying high-redshift galaxy clusters. Since the Compton  $y$ -parameter (the integral of the ICM pressure along the line-of-sight) does not diminish with distance, and since the CMB has a nearly uniform surface brightness, the SZ effect does not diminish with increasing redshift. This makes SZ surveys especially suitable for finding high redshift clusters (Planck Collaboration VIII 2011). These cluster samples can be used to constrain cosmological models (e.g., from the evolution of the mass function) and to probe the physics of structure formation (e.g., from cluster scaling relations and structural properties, Planck Collaboration VIII 2011). Many ongoing experiments are measuring the SZ effect; for instance, the South Pole Telescope (SPT, Carlstrom et al. 2011) and the Atacama Cosmology Telescope (ACT, Marriage et al. 2011) are each measuring tens to hundreds of clusters over a few hundred square degrees (Haiman, Mohr & Holder 2001; Weller, Battye & Kneissl 2002; Levine, Schulz, & White 2002; Majumdar & Mohr 2004; Douspis, Aghanim & Langer 2006; Shaw, Rudd & Nagai 2012).

With the mission to precisely measure CMB temperature and polarization anisotropy, the *Planck* satellite was successfully launched by the European Space Agency (ESA) on 14 May 2009 (Planck Collaboration 2005). *Planck* carries a scientific payload consisting of 74 detectors sensitive to frequencies between 25 and 1000 GHz. *Planck* scans the sky continuously with an angular resolution between about 30 arcmin (FWHM) at the lowest frequency to about 4 arcmin at the highest (Planck Collaboration VIII 2011). Its combination of frequency coverage, sensitivity, and angular resolution, enables it to measure the spatial anisotropy of the CMB with an accuracy set by fundamental astrophysical limits.

Performing an SZ cluster survey over the full sky was an important goal for *Planck* (Aghanim et al. 1997), and the Project produced its Early Release Compact Source Catalog (ERCSC, Planck Collaboration VII 2011) in 2011. The ERCSC included a catalog of 189 SZ clusters detected with high-reliability from the first ten months of the *Planck* survey<sup>3</sup>. The Project is ultimately expected to release a few thousand high-reliability SZ clusters (Planck Collaboration XII 2011).

The *WMAP* mission was launched by NASA on 30 June 2001 to map the CMB anisotropy over the full sky to multipole moment  $\ell \sim 1000$  (angular resolution  $\sim 0.2^\circ$ ). *WMAP* has precisely measured the cosmological parameters to unprecedented accuracy, but its angular resolution and frequency coverage (23 to 94 GHz) were not optimized for SZ detection. *WMAP* independently detected a dozen SZ clusters, all of which were well-known (Komatsu et al. 2011). It is therefore interesting and important to see if the SZ clusters detected by *Planck* are also detected in the 7-yr *WMAP* data. This is the aim of this paper.

The plan of this paper is as follows. In Section 2, we review the main features of the SZ effect and discuss the universal pressure profile we use to model the ICM pressure. In Section 3, we review the *Planck* ESZ catalog and the *WMAP* W-band data which form the basis of our analysis. In Section 4, we present the matched filter we apply to the *WMAP* sky map and examine the filtered model profiles for a range of cluster parameters. We present our main results in Section 4.3, and some concluding remarks follow.

Throughout this paper, we adopt a fiducial flat  $\Lambda$ CDM cos-

<sup>1</sup> Department of Physics and Astronomy, University of British Columbia, Vancouver, BC, V6T 1Z1, Canada

<sup>2</sup> Canadian Institute for Theoretical Astrophysics, Toronto, Canada

<sup>3</sup> Planck ERCSC website: <http://www.rssd.esa.int/Planck>

mology with Hubble constant  $H_0 = 70 \text{ km s}^{-1} \text{ Mpc}^{-1}$ , and matter density parameter  $\Omega_m = 0.3$ . The Hubble parameter at redshift  $z$  is  $H(z) = H_0 E(z)$ , where  $E^2(z) = \Omega_m(1+z)^3 + \Omega_\Lambda$ .

## 2. CLUSTER PRESSURE PROFILE

### 2.1. SZ effect

The thermal SZ effect is a secondary anisotropy in the the cosmic microwave background (CMB) radiation, caused by CMB photons scattering off free electrons in the hot ICM through the inverse Compton effect. The effect boosts the photon's energy and thus distorts the CMB spectrum, causing a temperature decrement on the low frequency side of the CMB peak, and vice versa. The induced temperature anisotropy in the direction of a cluster is (Sunyaev & Zeldovich 1972; Birkinshaw 1999; Carlstrom et al. 2002)

$$\frac{\Delta T}{T} = \left[ \eta \frac{e^\eta + 1}{e^\eta - 1} - 4 \right] y \equiv g_\nu y, \quad (1)$$

where  $g_\nu \equiv [\eta(e^\eta + 1)/(e^\eta - 1)] - 4$  captures the frequency dependence, and

$$\eta = \frac{h\nu}{k_B T_{\text{CMB}}} = 1.76 \left( \frac{\nu}{100 \text{ GHz}} \right). \quad (2)$$

The dimensionless Comptonization parameter  $y$  depends on the electron temperature,  $T_e(\mathbf{r})$ , and density,  $n_e(\mathbf{r})$ , in the ICM,

$$y = \int n_e(\mathbf{r}) \sigma_T \frac{k_B T_e(\mathbf{r})}{m_e c^2} dl, \quad (3)$$

where  $\sigma_T$  is the Thomson cross section,  $k_B$  is the Boltzmann constant,  $m_e$  is the electron rest mass and the integral is taken along the line of sight. Since  $y$  is positive, the sign of  $g_\nu$  determines whether  $\Delta T$  is an increment or decrement in the CMB temperature. With  $T_{\text{CMB}} = 2.725 \text{ K}$ , we have  $g_\nu > 0$  for  $\nu > 217 \text{ GHz}$ , and vice versa, and  $g_\nu \rightarrow -2$  at low frequencies ( $\eta \ll 1$ ).

It is convenient to define the integrated SZ signal as  $Y \equiv \int y d\Omega$ , where the integration is over the solid angle of the cluster. This is equivalent to a volume integral

$$Y = \frac{1}{D_A^2} \frac{\sigma_T}{m_e c^2} \int P dV, \quad (4)$$

where  $D_A$  is the angular diameter distance to the system and  $P = n_e k T_e$  the electron pressure (Planck Collaboration VIII 2011). In the following, we denote the integral performed over the sphere of radius  $R_{500}^4$  ( $5R_{500}$ ), as  $Y_{500}$  ( $Y_{5R500}$ ). Note that  $Y$  has units of solid angle, typically  $\text{arcm}^2$ .

### 2.2. Universal profile

In order to study the SZ effect in the WMAP data, we need a model for the pressure profile of the cluster gas,  $P(\mathbf{r})$ . Arnaud et al. (2010) studied ICM pressure profiles using a sample of 33 local ( $z < 0.2$ ) clusters observed with *XMM-Newton*. The sample spans a mass range of  $10^{14} M_\odot < M_{500} < 10^{15} M_\odot$ , where  $M_{500}$  is the mass enclosed within  $R_{500}$  (assumed to be spherically symmetric). The pressure profiles in their sample can be described by a universal profile that is scaled with both mass- and redshift-dependent factors. The

dispersion of the data about the scaled profile is less than 30% beyond  $0.2R_{500}$  (Arnaud et al. 2010).

With  $x \equiv r/R_{500}$ , the form of the universal profile given by Arnaud et al. (2010) is

$$P(x) = 1.65 \times 10^{-3} E(z)^{\frac{2}{3}} \left[ \frac{M_{500}}{3 \times 10^{14} M_\odot h_{70}^{-1}} \right]^{\frac{2}{3} + \alpha_p + \alpha'_p} \times \tilde{p}(x) h_{70}^2 \text{ [keV cm}^{-3}\text{]}, \quad (5)$$

where  $h_{70} = (h/0.7)$ ,  $\alpha_p = 0.12$ , and

$$\alpha'_p = 0.1 - (\alpha_p + 0.1) \frac{(x/0.5)^3}{1 + (x/0.5)^3}. \quad (6)$$

Here  $\tilde{p}(x)$  is the generalized NFW model proposed by Nagai, Kravtsov & Vikhlinin (2007) (see also Arnaud et al. 2010)

$$\tilde{p}(x) = \frac{P_0}{(c_{500} x)^\gamma [1 + (c_{500} x)^\alpha]^{(\beta - \gamma)/\alpha}}, \quad (7)$$

where  $P_0 = 8.403 h_{70}^{-3/2}$  is the overall magnitude of the pressure profile, and  $c_{500}$ ,  $\gamma$ ,  $\alpha$ , and  $\beta$  determine the slope of the profile. By fitting this pressure template to the simulated profile, Arnaud et al. (2010) found the best parameters are  $c_{500} = 1.177$ ,  $\gamma = 0.3081$ ,  $\alpha = 1.051$ , and  $\beta = 5.4905$ .

The only parameter left undetermined in Eq. (5) is the mass parameter  $M_{500}$ , which is nearly degenerate with the overall pressure normalization term  $P_0$  in Eq. (7). To illustrate this degeneracy, we plot in Fig. 1a the normalized pressure profiles,  $P(x)/P(0)$ , for several combinations of  $M_{500}$  and cluster redshift,  $z$ . They show very similar normalized profiles.

The angular profile of the model SZ signal is obtained by projecting the 3-D pressure profile  $P(\mathbf{r})$  onto the plane of the sky and calculating the corresponding temperature profile. Following Komatsu et al. (2011), the projected profile, in  $\text{keV cm}^{-3}$ , is

$$P_{2d}(\theta) = \int_{-\sqrt{r_{\text{out}}^2 - \theta^2 D_A^2}}^{\sqrt{r_{\text{out}}^2 - \theta^2 D_A^2}} P \left( \sqrt{l^2 + \theta^2 D_A^2} \right) dl, \quad (8)$$

where  $D_A$  is the angular diameter distance to redshift  $z$ , and  $r_{\text{out}}$  is the truncated radius, which we take to be  $r_{\text{out}} = 6R_{500}$ . Beyond this range, the projection is not very sensitive to  $r_{\text{out}}$  because the profile falls off rapidly.

Given the 2-dimensional pressure profile, the temperature profile is

$$\frac{\Delta T_{\text{SZ}}(\theta)}{T} = g_\nu \frac{\sigma_T}{m_e c^2} P_{2d}(\theta), \quad (9)$$

and the Comptonization parameter  $y$  (Eq. (3)) is

$$y(\theta) = \frac{\sigma_T}{m_e c^2} P_{2d}(\theta) = (8 \times 10^{-3}) \int_0^{\sqrt{(6\theta_{500})^2 - \theta^2} \bar{D}_A} dx \times P \left( \sqrt{\left( \frac{x}{\theta_{500} \bar{D}_A} \right)^2 + \left( \frac{\theta}{\theta_{500}} \right)^2} \right), \quad (10)$$

where we have used  $\theta \equiv r/D_A$ .

In Fig. 1b, we plot the normalized Comptonization profile,  $y(\theta)/y(0)$  vs.  $\theta/\theta_{500}$ , for the same four cluster parameters as in Fig. 1a. Again, the normalized  $y$  profiles are very similar.

<sup>4</sup>  $R_{500}$  is defined as the radius within which the density contrast is  $> 500$ .

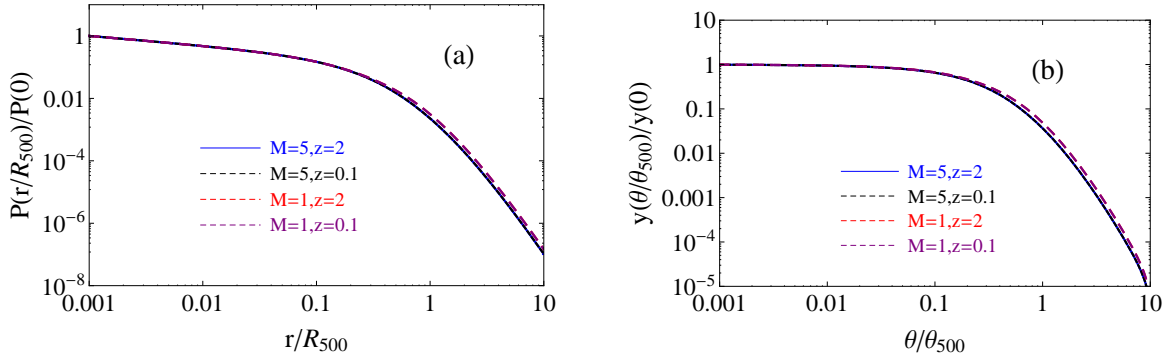


FIG. 1.— *Left* – Pressure profile from Eq. (5) for four hypothetical clusters. *Right* – The temperature profile from Eq. (10) for the same four cluster parameters. The units of  $M$ ,  $R_{500}$ , and  $\theta_{500}$  are  $3 \times 10^{14} h_{70}^{-1} M_{\odot}$ , Mpc, and arcmin, respectively, where  $h_{70} = (h/0.7)$ .

Since we fit the normalization of the profile to the *WMAP* data, we are primarily concerned with the angular radius of each cluster,  $\theta_{500}$ , which scales the extent of the profile. As discussed below, this parameter may be derived from information provided in the *Planck* ESZ catalog. Thus, when fitting the *WMAP* data, we adopt the normalized profile in Eq. (10), using the  $\theta_{500}$  value predicted by *Planck*.

### 3. DATA DESCRIPTION

In this section, we introduce the data used in our analysis: the *Planck* Early SZ catalog, which consists of 189 clusters; and the *WMAP* W-band sky map that will be used for consistency testing.

#### 3.1. *Planck* ESZ catalog

*Planck* is a full-sky CMB survey with nine different frequency channels, 30, 44, 70, 100, 143, 217, 353, 545, and 857 GHz. The FWHM angular resolution for these channels are 33, 24, 14, 10, 7.1, 5, 5 and 5 arcmin, respectively (Planck Collaboration 2005).

The ESZ catalog was obtained from a blind, multi-frequency search of the *Planck* High Frequency Instrument (HFI) maps, using an all-sky extension of the algorithm given in Melin et al. (2006). The team used a matched multi-frequency filter method to enhance signal-to-noise in the 189 detected objects; the filter optimizes detectability by using a linear combination of frequency maps to null the CMB signal, and spatial filtering to suppress foregrounds and instrument noise (Planck Collaboration VIII 2011). Therefore, the *Planck* filter boosts the expected SZ signal over all-sky emission (including foregrounds) and noise. In principle, SZ clusters can be also seen in the three Low Frequency Instrument (LFI) channels; however, the low-frequency beam size ( $\sim 25$  arcmin) is generally much larger than a typical cluster size of  $\sim 5$  arcmin, effectively diluting the signal, and therefore the LFI channels were not included in the analysis (Planck Collaboration VIII 2011). The position and radius ( $5R_{500}$ ) of each cluster profile was varied to maximize the signal-to-noise ratio of each detection. The position, angular radius,  $5\theta_{500}$ , and integrated Comptonization parameter,  $Y_{5R500}$ , are tabulated for each cluster in the catalog (Planck Collaboration VIII 2011)<sup>5</sup>.

<sup>5</sup> With the assumption of spherical symmetry in the model profile, we have  $Y_{5R500} = 1.8 \times Y_{500}$ .

The preliminary analysis yielded 201 high signal-to-noise ( $S/N > 6$ ) candidates, of which 189 were deemed to be of high reliability. Of these, 169 were already known from X-ray and optical surveys, while 20 clusters were newly detected. The new clusters were subsequently confirmed by *XMM-Newton* observations (Planck Collaboration IX 2011) and by the Arcminute Microkelvin Imager (AMI) survey (Zwart et al. 2008).

Redshifts are known for 175 of the 189 clusters. Since we require redshift information to construct a pressure profile, we limit our analysis of *WMAP* data to this subset of the full catalog. The redshift distribution and positions of the *Planck* ESZ clusters are shown in Fig. 2: in panel (a), the redshift distribution of these clusters is seen to range from 0.01 to 0.5 with a mean redshift of 0.18. Their spatial distribution shown in panel (b) is close to uniform across the sky, outside a  $|b| < 14^\circ$  Galaxy cut, although in principle more objects are sampled around the ecliptic poles.

#### 3.2. *WMAP* W-band data

The *WMAP* satellite produced full-sky maps at five frequency bands from 23 to 94 GHz, with a FWHM angular resolution from 52.8 to 13.2 arcmin, respectively. These maps were used to measure cosmological parameters with unprecedented accuracy.

Taking into account the combined effects of spectral shape,  $g_\nu$ , and diffraction-limited beam size, the largest SZ decrement occurs around 140 GHz (Carlstrom et al. 2002), which is higher than the highest *WMAP* frequency. Within the *WMAP* bands, the 94 GHz W-band map has the most sensitivity to SZ signal, owing mostly to its angular resolution (and relatively low foreground contamination). We use the W-band HEALPIX map at  $n_{\text{side}} = 1024$  (Gorski et al. 2005). In the following analysis, we fit SZ profiles to the 7-yr W-band sky map. At 94 GHz, the SZ decrement is  $\Delta T_{\text{SZ}}/T = -1.56y$ .

### 4. FILTERING TECHNIQUE

To optimally characterize the SZ signal, we need to filter the observed maps, which are dominated by primary CMB fluctuations, but which also include residual foreground signals (including extragalactic point sources) and instrument noise. In this section we describe the choice of filter (following Tegmark & de Oliveira-Costa 1998), calculate the temperature profile of SZ clusters after filtering, and compute the  $Y$ -parameter. We then compare  $Y_{500}$  derived from *WMAP* with that derived from *Planck*.

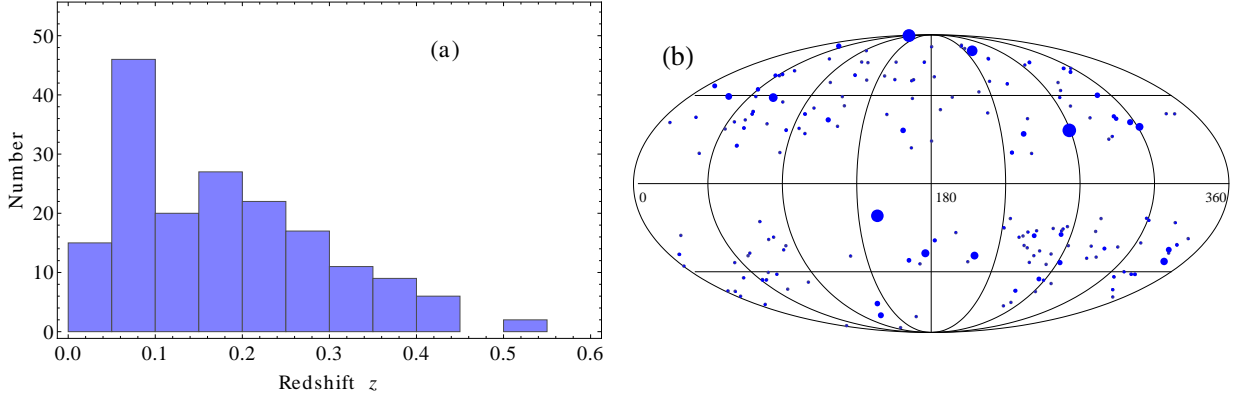


FIG. 2.— *Left* – redshift histogram of 175 *Planck* ESZ clusters. *Right* – full-sky distribution of *Planck* ESZ clusters; the size of each point is proportional to the angular radius  $\theta_{500}$ .

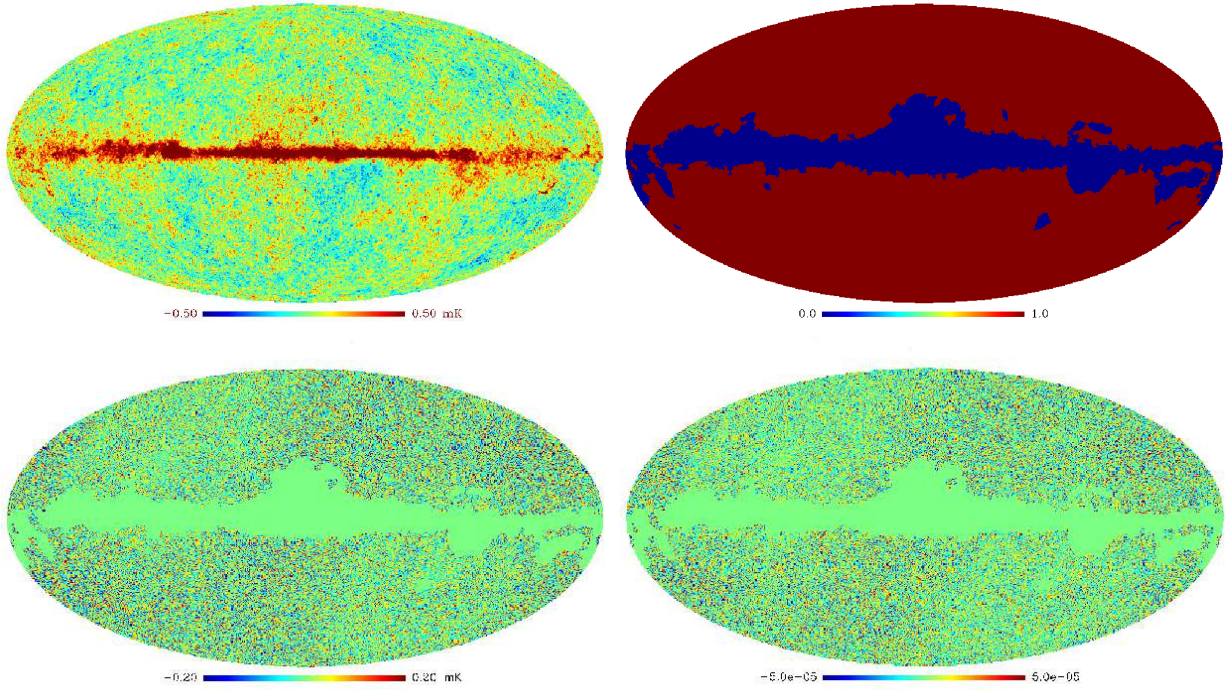


FIG. 3.— *WMAP* data used in this analysis. *Upper-left* – co-added 7-yr W-band map. *Upper-right* – *WMAP* 7-yr analysis mask, including point source cuts, 82.4% of the sky remains. *Lower-left* – filtered W-band temperature map, as per Eq. (15). *Lower-right* – dimensionless  $y$ -parameter map, as per Eq. (10).

#### 4.1. Optimal filter

SZ clusters are typically unresolved in the *WMAP* beam, so we treat them as point sources on the sky. In this limit, if cluster  $i$  has flux  $S_i$  at sky position  $\hat{r}_i$ , the sky temperature  $\Delta T(\hat{r})$  may be written as

$$\Delta T(\hat{r}) = c \sum_i S_i \delta(\hat{r}, \hat{r}_i) + \sum_{\ell m} a_{\ell m} Y_{\ell m}(\hat{r}), \quad (11)$$

where  $\delta$  is the Dirac delta function, and  $c$  is the conversion factor between flux and temperature, given by

$$c = c_* \frac{[2 \sinh(\frac{\eta}{2})]^2}{\eta^4}, \quad c_* = \frac{1}{2k_B} \left( \frac{hc}{kT_{\text{CMB}}} \right)^2 \simeq \frac{10 \text{ mK}}{\text{MJy sr}^{-1}}, \quad (12)$$

where  $\eta$  is defined in Eq. (2) (see also Tegmark & Efstathiou 1996; Tegmark & de Oliveira-Costa 1998). Here, the spherical harmonic coefficients  $a_{\ell m}$  characterize the true CMB tem-

perature fluctuation. The sky signal convolved with the beam response,  $B_\ell$ , is

$$\Delta T^{\text{obs}}(\hat{r}) = c \sum_i S_i \left( \sum_{\ell} \frac{2\ell+1}{4\pi} P_\ell(\hat{r} \cdot \hat{r}_i) B_\ell \right) + \sum_{\ell m} a_{\ell m}^{\text{tot}} Y_{\ell m}(\hat{r}). \quad (13)$$

Here  $a_{\ell m}^{\text{tot}}$  encodes the temperature due to CMB fluctuations (convolved with the beam), and detector noise (not convolved with the beam),

$$a_{\ell m}^{\text{tot}} = a_{\ell m}^{\text{CMB}} B_\ell + n_{\ell m}, \quad (14)$$

where the beam transfer function,  $B_\ell$ , is obtained from the LAMBDA website. [Note: in this analysis, we use the *WMAP* 7-yr W-band map supplied by the *WMAP* team (Fig. 3 upper-

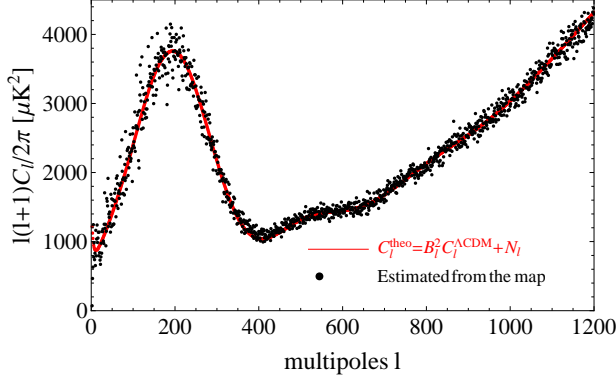


FIG. 4.— Measured (black) and predicted (red) power spectra,  $C_\ell$ , from the WMAP 7-yr W-band map. The predicted spectrum is based on the best-fit  $\Lambda$ CDM model convolved with the beam, plus detector noise, assuming  $N_\ell \equiv 0.0187 \mu\text{K}^2$  (Hinshaw et al. 2007).

left), and impose the WMAP 7-yr analysis mask (Fig. 3 upper-right); we also neglect residual foreground signals in the cleaned, masked maps.] Fig. 4 compares the angular power spectrum,  $C_\ell$ , directly estimated from the map with the spectrum predicted by Eq. (14) using the best-fit  $\Lambda$ CDM model. The predicted spectrum agrees with the measured spectrum very well.

To maximize our sensitivity to point sources, we further convolve the observed map  $\Delta T^{\text{obs}}$  with an optimal filter  $W_\ell$ , so that

$$\Delta \tilde{T}(\hat{r}) = c \sum_i S_i \left( \sum_\ell \frac{2\ell+1}{4\pi} P_\ell(\hat{r} \cdot \hat{r}_i) B_\ell W_\ell \right) + \sum_{\ell m} a_{\ell m}^{\text{tot}} W_\ell Y_{\ell m}(\hat{r}). \quad (15)$$

Note that this form implicitly assumes that the beam response and optimal filter are both azimuthally symmetric. Treating the second line in Eq. (15) as the noise term, we seek the form of  $W_\ell$  that maximizes the cluster signal-to-noise ratio. In the direction of cluster  $i$ , the filtered signal is  $\Delta \tilde{T}(\hat{r}_i) = AS_i$ , where

$$A \equiv c \sum_\ell \frac{2\ell+1}{4\pi} B_\ell W_\ell = \text{constant}. \quad (16)$$

We choose  $W_\ell$  to minimize the ratio

$$\sigma^2 = \text{Var} \left( \frac{\Delta \tilde{T}}{A} \right) = \frac{\sum_\ell \frac{2\ell+1}{4\pi} C_\ell^{\text{tot}} W_\ell^2}{c^2 \left( \sum_\ell \frac{2\ell+1}{4\pi} B_\ell W_\ell \right)^2}, \quad (17)$$

where  $C_\ell^{\text{tot}} \equiv B_\ell^2 C_\ell^{\text{CMB}} + N_\ell$ , and we take  $C_\ell^{\text{CMB}}$  to be the  $\Lambda$ CDM model power spectrum.

We minimize Eq. (17) by adding a Lagrange multiplier to the numerator,

$$\sum_\ell \frac{2\ell+1}{4\pi} C_\ell^{\text{tot}} W_\ell^2 + \lambda \left( \sum_\ell \frac{2\ell+1}{4\pi} B_\ell W_\ell \right)^2, \quad (18)$$

and minimizing with respect  $W_\ell$ . We obtain

$$W_\ell \sim \frac{B_\ell}{B_\ell^2 C_\ell^{\text{CMB}} + N_\ell} = \frac{B_\ell}{C_\ell^{\text{tot}}}. \quad (19)$$

The normalization of  $W_\ell$  does not affect the signal-to-noise ratio of the cluster detection. We plot  $W_\ell$  in Fig. 5; note that

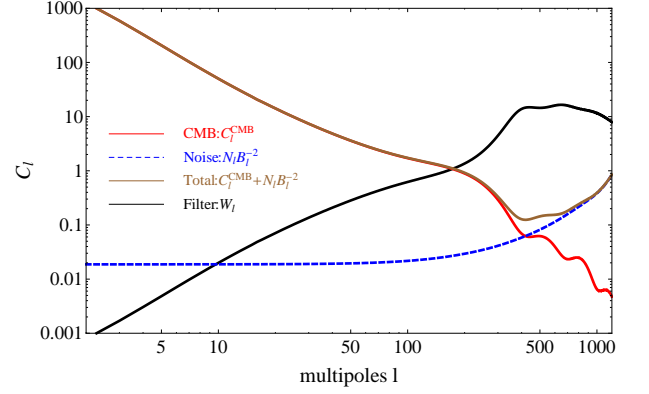


FIG. 5.— Optimal filter (black) for point source detection in the WMAP 7-yr W-band map, Eq. (19). The CMB signal (red line) and detector noise (dashed blue line) are shown for comparison, along with their sum (brown line).

$W_\ell$  is maximal in the range  $\ell \sim 500 - 1000$ . With this filter, the smallest variance we can obtain for a point source is

$$\sigma^2 = c^{-2} \left( \sum_\ell \frac{2\ell+1}{4\pi} \frac{B_\ell^2}{C_\ell^{\text{tot}}} \right)^{-1}. \quad (20)$$

#### 4.2. The filtered cluster profile

What is the shape of the universal cluster profile after filtering? Let the unfiltered temperature map due to  $N$  clusters at positions  $\hat{r}_i$  ( $i = 1, \dots, N$ ) be

$$x(\hat{r}) = \sum_i f_i(\Theta_i), \quad (21)$$

where  $f_i$  is the profile of the  $i$ th cluster, and  $\Theta_i$  is the angle between the  $i$ th cluster and  $\hat{r}$ ,

$$\cos \Theta_i = \hat{r}_i \cdot \hat{r} = \cos \theta_i \cos \theta + \sin \theta_i \sin \theta \cos(\phi - \phi_i). \quad (22)$$

The filtered cluster map may be written as

$$\begin{aligned} \tilde{x}(\hat{r}) &= (W * x)(\hat{r}) \\ &= \sum_i \left[ \int d\Omega' f_i(\Theta') W(\cos \Theta') \right], \end{aligned} \quad (23)$$

where

$$W(\cos \Theta') = \sum_\ell \frac{2\ell+1}{4\pi} W_\ell P_\ell(\cos \Theta'), \quad (24)$$

and  $\cos \Theta' = \hat{r} \cdot \hat{r}'$ . In the limit that the SZ clusters can be considered point sources,  $f_i(\Theta_i) = c S_i \delta(\hat{r}_i, \hat{r})$ , the filtered map reduces to

$$\tilde{x}(\hat{r}) = c \sum_i S_i \sum_\ell \frac{2\ell+1}{4\pi} W_\ell P_\ell(\cos \Theta_i). \quad (25)$$

In Fig. 6, we plot selected SZ cluster profiles before and after filtering. For the small cluster case shown in Fig. 6a, the filtered profile does not differ appreciably from a filtered point source, because the cluster is unresolved. However, for larger cluster (Fig. 6b), the filtered profile is noticeably different from a filtered point source profile. In either case, we note that  $\theta_{500}$  lies within the radius where the filtered profile is still positive, so this filter should not suppress actual SZ signal. We consider this question in more detail in the following section.

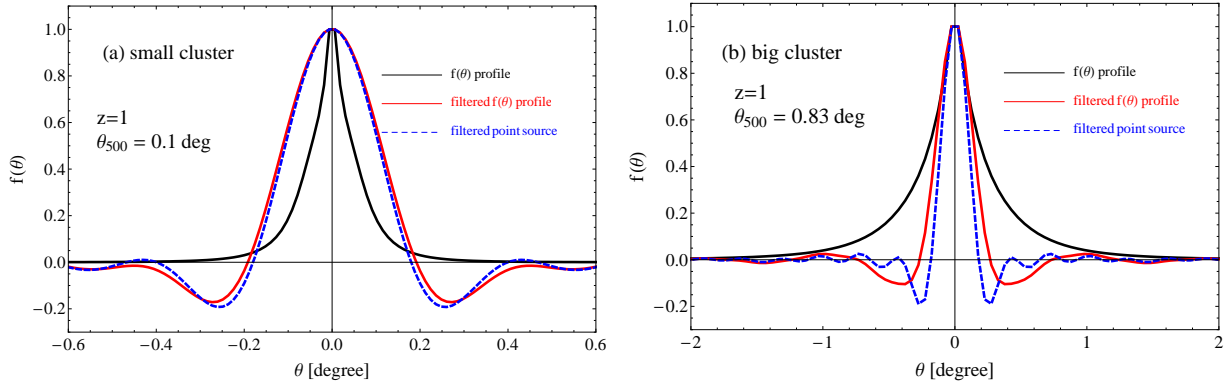


FIG. 6.— Shape of selected cluster profiles before and after filtering. *Left* – a small cluster with  $\theta_{500}$  less than the *WMAP* W-band beam size,  $0.22^\circ$ ; *Right* – a marginally resolved cluster.

### 4.3. Results of filtering

In Fig. 3 lower-left panel, we show the filtered *WMAP* 7-yr W-band map, which exhibits suppression of CMB signal over a range of angular scales. The dimensionless  $y$ -map obtained from  $y = -\Delta T_{\text{SZ}}/(1.56T)$  is shown in the lower-right panel of Fig. 3. We then calculate  $Y_{500}$  for each cluster. To do this, we use  $R_{500}$  as the radius of each cluster and sum over all of the pixels within this radius, i.e.,

$$Y_{500} = \sum_{i}^{R \leq R_{500}} y(\hat{r}_i). \quad (26)$$

We then tabulate the results in column 8 of Table 2. To evaluate the uncertainty in  $Y_{500}$ , we simulate 1000 sky maps with CMB signal and pixel noise. For each map we calculate  $Y_{500}$  at each cluster position, then compute the standard deviation over the ensemble of maps. The resulting error is given in column 9 of Table 2.

Because of beam dilution and detector noise in the *WMAP* data, the signal-to-noise ratio for the detection of individual SZ clusters is relatively low; however, the stacked signal is detected at high significant level. In Table 1 we give the aggregate signal-to-noise ratio for two methods of stacking: unweighted and weighted. In the first method we evaluate

$$\frac{\sum_i Y_i}{(\sum_i \delta Y_i^2)^{1/2}}, \quad (27)$$

which equally weights all cluster detections. The total signal-to-noise ratio for this method is 8.9 for *WMAP* and 85.2 for *Planck*. In the second method we evaluate

$$\left[ \sum_i \left( \frac{Y_i}{\delta Y_i} \right)^2 \right]^{1/2}, \quad (28)$$

which down-weights clusters with low signal-to-noise. This gives an aggregate signal-to-noise of 16.3 for *WMAP* and 123.3 for *Planck*. In Fig. 7 we show the aggregate SZ profile from the stacked *WMAP* data and compare this to the predicted profile based on stacking the universal pressure profile, scaled by the measured Comptonization parameters from the *Planck* catalog.

Next, we assess the consistency between the *WMAP* and *Planck* cluster detections. Figure 8 compares the integrated Comptonization parameter,  $Y_{500}$ , from each data set. While there is quite a bit of scatter, the two measurements are clearly

TABLE 1  
AGGREGATE SIGNAL-TO-NOISE FOR STACKED SZ CLUSTERS

Method	<i>WMAP</i>	<i>Planck</i>
unweighted, Eq. (27)	8.9	85.2
weighted, Eq. (28)	16.3	123.3

correlated. We use linear regression with errors in both axes to fit the slope between the two data sets (see Appendix A). Using Eq. (A5), we find

$$Y_{500}^{\text{wmap}} = (1.23 \pm 0.18) \times Y_{500}^{\text{planck}} \quad (68\% \text{ CL}), \quad (29)$$

which is within  $2\sigma$  of unity. Fig. 8 shows the best-fit regression in red.

While the measured slope is perfectly consistent with unity, we briefly consider some potential sources of systematic error in our comparison. (1) The amplitude of  $Y_{500}^{\text{wmap}}$  depends on how one treats the monopole moment in the *WMAP* map. In our analysis, we subtract the monopole both before and after we apply the optimal filter to the map. (2) Finite pixel size can introduce noise when identifying pixels within an area that is not much larger than the pixel size. We account for this effect in our Monte Carlo evaluation of the  $Y_{500}^{\text{wmap}}$  uncertainty. (3) For clusters with  $\theta_{500}$  larger than the *WMAP* W-band beam width of  $0.21^\circ$ , the integral for  $Y_{500}$  includes some negative regions in the filtered profile, as shown in Fig. 6. This will suppress the integrated signal in those clusters. The smaller value of  $Y_{500}^{\text{wmap}}$  measured in the Coma cluster, compared to  $Y_{500}^{\text{planck}}$ , is due to this effect. We note that our value is consistent with that reported by Komatsu et al. (2011)<sup>6</sup>. (4) While the *Planck* team documented their detection of SZ clusters (Planck Collaboration VIII 2011; Planck Collaboration VII 2011; Planck Collaboration IX 2011), some processing details are not explicitly described, such as the precise choice of filter. Despite these uncertainties, the best-fit slope between  $Y_{500}^{\text{wmap}}$  and  $Y_{500}^{\text{planck}}$  is consistent with unity and suggests that such effects are not significant.

## 5. CONCLUSION

<sup>6</sup> Komatsu et al. (2011) do not give an explicit value for  $Y_{500}$ , but from the measured dimensionless quantity  $y \sim 7 \times 10^{-5}$  (two equations after their equation (71)), and the profile width of  $10.3'$  (three lines above their equation (70) and figure 14), we estimate that their measured value of  $Y_{500}$  for COMA would be about  $0.01 \text{ arcmin}^2$ , which is consistent with our finding, within the errors.

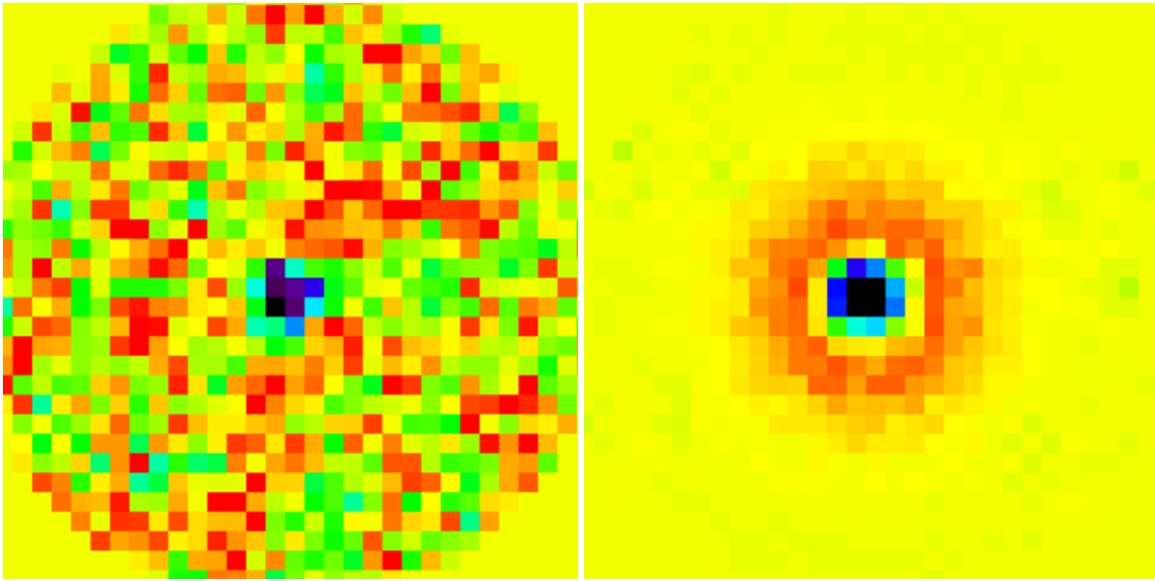


FIG. 7.— *Left* – Average SZ profile map obtained from stacking the WMAP 7-yr filtered W-band data at the locations of the 175 SZ clusters in the *Planck* ESZ catalog. The color scale ranges from  $-4$  mK (black) to  $+1$  mK (red). *Right* – The corresponding prediction based on stacking the universal pressure profile scaled by the *Planck*-measured Comptonization parameter,  $Y_{500}$ . The “Mexican-hat” like ring is the results of applying the matched filter.

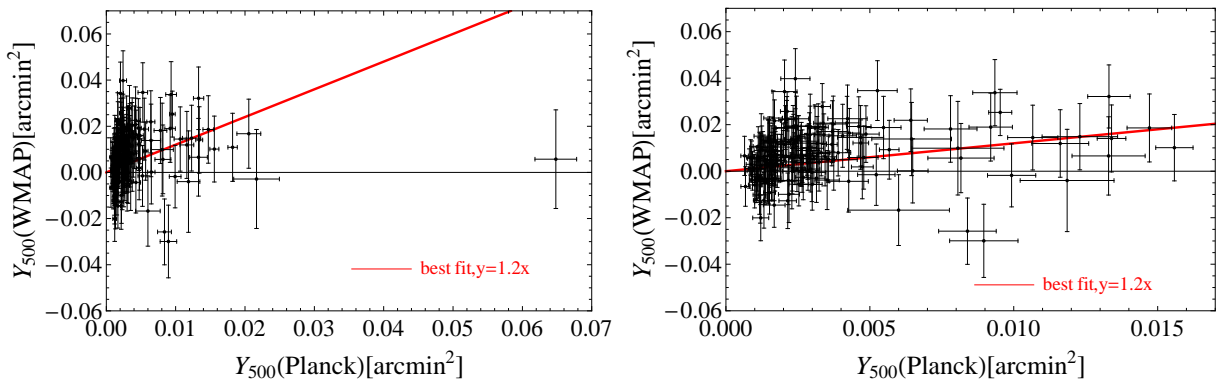


FIG. 8.— Comparison of 175 individual SZ cluster measurements,  $Y_{500}$ , from WMAP and *Planck*. The left panel shows the comparison at full scale, while the right panel zooms in to a smaller  $Y_{500}$  range. We use the relation  $Y_{500} \simeq Y_{5R500}/1.8$  to obtain  $Y_{500}$  from the *Planck* catalog.

The *Planck* collaboration released its ESZ cluster catalog in Jan 2011. It contained 189 SZ clusters across the full sky, 175 of which had tabulated redshifts. In this paper, we examine these 175 cluster locations in the WMAP data to assess consistency with the *Planck* catalog.

We assume that the clusters are described by a universal pressure profile, Eq. (5), and project the 3-D profile onto the plane of the sky. Given this profile, we can calculate the integrated Comptonization parameter,  $Y_{500}$ , for any cluster location determined by *Planck*. We filter the WMAP 7-yr W-band data with an optimal filter to suppress primary CMB signal and detector noise, then examine the effects of the filter on the universal pressure profile. We conclude that the angular radius,  $\theta_{500}$ , adequately captures the bulk of the SZ signal in the filtered data. We estimate the uncertainty in  $Y_{500}$  using 1000 Monte Carlo realizations of a  $\Lambda$ CDM CMB signal plus detector noise.

We perform two consistency tests between  $Y_{500}^{\text{wmap}}$  and  $Y_{500}^{\text{planck}}$ . First, we stack all the cluster data to estimate the total signal-to-noise ratio. In the weighted stacking, we obtain an aggregate signal-to-noise ratio of 16.3 from the WMAP data, which clearly indicates that WMAP detects the most signifi-

cant clusters seen by *Planck*.

Next we compare  $Y_{500}^{\text{wmap}}$  and  $Y_{500}^{\text{planck}}$  for each cluster. In a linear regression analysis, which accounts for errors in both measurements, we find the best-fit slope is  $1.23 \pm 0.18$ . This is consistent with unity at the  $2\sigma$  confidence level. We further consider some systematic error sources that could lead to a slope slightly greater than unity. Our results show that there are no fundamental problems with reliability of the ESZ or the calibration of the SZ amplitude. A similar conclusion was also drawn in the third version of Whitbourn, Shanks & Sawangwit (2011).

The filtering technique presented here could easily be extended to other surveys, such as ACT and SPT. We plan to revisit this issue when the appropriate data are publicly available.

#### ACKNOWLEDGMENTS

The authors acknowledge the use of the LAMBDA Data Center (<http://lambda.gsfc.nasa.gov/>). We thank Kris Sigurdson and Jim Zibin for helpful discussions. This research was supported by the Natural Sciences and Engineering Research Council of Canada. Y.Z.M is supported by a CITA National





TABLE 2  
WMAP OBSERVATIONS OF *Planck* ESZ CLUSTERS

Index	Gal lon ( <i>l</i> ) (deg)	Gal lat ( <i>b</i> ) (deg)	Redshift	$\theta_{500}$ (arcmin)	$Y_{500}^{\text{planck}}$ (arcmin <sup>2</sup> )	$\delta Y_{500}^{\text{planck}}$ (arcmin <sup>2</sup> )	$Y_{500}^{\text{wmap}}$ (arcmin <sup>2</sup> )	$\delta Y_{500}^{\text{wmap}}$ (arcmin <sup>2</sup> )
1	0.4409	-41.8351	0.1651	6.3071	$0.14 \times 10^{-2}$	$0.27 \times 10^{-3}$	$0.48 \times 10^{-2}$	$0.92 \times 10^{-2}$
2	2.7497	-56.1827	0.1411	7.1114	$0.17 \times 10^{-2}$	$0.27 \times 10^{-3}$	$0.71 \times 10^{-2}$	$0.10 \times 10^{-1}$
3	3.9081	-59.4171	0.1510	7.6784	$0.33 \times 10^{-2}$	$0.28 \times 10^{-3}$	$0.27 \times 10^{-1}$	$0.10 \times 10^{-1}$
4	6.4760	50.5490	0.0766	15.5982	$0.99 \times 10^{-2}$	$0.84 \times 10^{-3}$	$-0.18 \times 10^{-2}$	$0.14 \times 10^{-1}$
5	6.7046	-35.5407	0.0894	10.5796	$0.32 \times 10^{-2}$	$0.44 \times 10^{-3}$	$0.39 \times 10^{-2}$	$0.13 \times 10^{-1}$
6	6.7849	30.4683	0.2030	7.5616	$0.95 \times 10^{-2}$	$0.40 \times 10^{-3}$	$0.25 \times 10^{-1}$	$0.10 \times 10^{-1}$
7	8.3005	-64.7564	0.3120	8.7664	$0.27 \times 10^{-2}$	$0.56 \times 10^{-3}$	$0.63 \times 10^{-2}$	$0.11 \times 10^{-1}$
8	8.4486	-56.3564	0.1486	6.7883	$0.13 \times 10^{-2}$	$0.26 \times 10^{-3}$	$-0.44 \times 10^{-2}$	$0.97 \times 10^{-2}$
9	8.9362	-81.2386	0.3066	4.6335	$0.23 \times 10^{-2}$	$0.27 \times 10^{-3}$	$0.19 \times 10^{-1}$	$0.87 \times 10^{-2}$
10	18.5314	-25.7228	0.3171	4.1424	$0.15 \times 10^{-2}$	$0.22 \times 10^{-3}$	$-0.52 \times 10^{-2}$	$0.84 \times 10^{-2}$
11	21.0918	33.2560	0.1514	9.0695	$0.42 \times 10^{-2}$	$0.41 \times 10^{-3}$	$0.20 \times 10^{-1}$	$0.11 \times 10^{-1}$
12	29.0054	44.5625	0.0353	21.7792	$0.82 \times 10^{-2}$	$0.12 \times 10^{-2}$	$0.56 \times 10^{-2}$	$0.15 \times 10^{-1}$
13	33.4614	-48.4318	0.0943	8.8429	$0.30 \times 10^{-2}$	$0.34 \times 10^{-3}$	$-0.56 \times 10^{-2}$	$0.11 \times 10^{-1}$
14	33.7814	77.1628	0.0622	17.1573	$0.93 \times 10^{-2}$	$0.77 \times 10^{-3}$	$0.33 \times 10^{-1}$	$0.13 \times 10^{-1}$
15	36.7219	14.9232	0.1525	7.0561	$0.19 \times 10^{-2}$	$0.34 \times 10^{-3}$	$0.58 \times 10^{-2}$	$0.98 \times 10^{-2}$
16	39.8595	-39.9889	0.1760	5.9780	$0.17 \times 10^{-2}$	$0.29 \times 10^{-3}$	$0.30 \times 10^{-2}$	$0.94 \times 10^{-2}$
17	42.8257	56.6172	0.0723	12.6087	$0.55 \times 10^{-2}$	$0.61 \times 10^{-3}$	$0.18 \times 10^{-1}$	$0.13 \times 10^{-1}$
18	44.2253	48.6842	0.0894	14.0653	$0.13 \times 10^{-1}$	$0.74 \times 10^{-3}$	$0.32 \times 10^{-1}$	$0.13 \times 10^{-1}$
19	46.0815	27.1816	0.3890	3.5573	$0.12 \times 10^{-2}$	$0.19 \times 10^{-3}$	$0.87 \times 10^{-2}$	$0.76 \times 10^{-2}$
20	46.5037	-49.4389	0.0846	10.8945	$0.35 \times 10^{-2}$	$0.42 \times 10^{-3}$	$-0.38 \times 10^{-2}$	$0.13 \times 10^{-1}$
21	46.8830	56.4988	0.1145	9.0824	$0.37 \times 10^{-2}$	$0.46 \times 10^{-3}$	$0.20 \times 10^{-1}$	$0.11 \times 10^{-1}$
22	48.0522	57.1769	0.0777	10.9294	$0.37 \times 10^{-2}$	$0.54 \times 10^{-3}$	$0.17 \times 10^{-1}$	$0.13 \times 10^{-1}$
23	49.2044	30.8618	0.1644	7.2635	$0.24 \times 10^{-2}$	$0.30 \times 10^{-3}$	$0.39 \times 10^{-2}$	$0.97 \times 10^{-2}$
24	49.3365	44.3823	0.0972	8.5539	$0.30 \times 10^{-2}$	$0.48 \times 10^{-3}$	$-0.52 \times 10^{-3}$	$0.11 \times 10^{-1}$
25	49.6670	-49.5094	0.0980	9.5536	$0.21 \times 10^{-2}$	$0.37 \times 10^{-3}$	$0.18 \times 10^{-1}$	$0.12 \times 10^{-1}$
26	53.4434	-36.2698	0.3250	1.6148	$0.98 \times 10^{-3}$	$0.19 \times 10^{-3}$	$0.12 \times 10^{-2}$	$0.59 \times 10^{-2}$
27	53.5227	59.5442	0.1130	8.8081	$0.31 \times 10^{-2}$	$0.43 \times 10^{-3}$	$0.53 \times 10^{-2}$	$0.11 \times 10^{-1}$
28	55.6010	31.8644	0.2240	6.1481	$0.27 \times 10^{-2}$	$0.26 \times 10^{-3}$	$-0.26 \times 10^{-2}$	$0.99 \times 10^{-2}$
29	55.9755	-34.8850	0.1244	6.7696	$0.20 \times 10^{-2}$	$0.28 \times 10^{-3}$	$0.65 \times 10^{-2}$	$0.98 \times 10^{-2}$
30	56.8121	36.3165	0.0953	10.6714	$0.32 \times 10^{-2}$	$0.40 \times 10^{-3}$	$0.75 \times 10^{-2}$	$0.12 \times 10^{-1}$
31	56.9685	-55.0798	0.4470	3.5090	$0.16 \times 10^{-2}$	$0.20 \times 10^{-3}$	$0.86 \times 10^{-2}$	$0.76 \times 10^{-2}$
32	57.2694	-45.3577	0.3970	4.3122	$0.18 \times 10^{-2}$	$0.21 \times 10^{-3}$	$0.68 \times 10^{-2}$	$0.86 \times 10^{-2}$
33	57.3362	88.0113	0.0231	40.6731	$0.65 \times 10^{-1}$	$0.30 \times 10^{-2}$	$0.56 \times 10^{-2}$	$0.21 \times 10^{-1}$
34	57.6138	34.9421	0.0802	10.4783	$0.29 \times 10^{-2}$	$0.39 \times 10^{-3}$	$0.37 \times 10^{-2}$	$0.13 \times 10^{-1}$
35	57.9289	27.6442	0.0757	11.7297	$0.20 \times 10^{-2}$	$0.43 \times 10^{-3}$	$0.34 \times 10^{-1}$	$0.13 \times 10^{-1}$
36	58.2818	18.5938	0.0650	12.5308	$0.48 \times 10^{-2}$	$0.50 \times 10^{-3}$	$0.58 \times 10^{-2}$	$0.13 \times 10^{-1}$
37	62.4239	-46.4150	0.0906	9.4655	$0.23 \times 10^{-2}$	$0.39 \times 10^{-3}$	$-0.41 \times 10^{-2}$	$0.12 \times 10^{-1}$
38	62.9261	43.7096	0.0299	27.6348	$0.13 \times 10^{-1}$	$0.13 \times 10^{-2}$	$0.65 \times 10^{-2}$	$0.16 \times 10^{-1}$
39	67.2317	67.4641	0.1712	7.4168	$0.31 \times 10^{-2}$	$0.30 \times 10^{-3}$	$-0.30 \times 10^{-2}$	$0.10 \times 10^{-1}$
40	71.6149	29.7983	0.1565	5.4367	$0.13 \times 10^{-2}$	$0.20 \times 10^{-3}$	$0.62 \times 10^{-2}$	$0.92 \times 10^{-2}$
41	72.6308	41.4639	0.2280	6.2793	$0.47 \times 10^{-2}$	$0.27 \times 10^{-3}$	$0.12 \times 10^{-1}$	$0.97 \times 10^{-2}$
42	72.8026	-18.7212	0.1430	7.4432	$0.28 \times 10^{-2}$	$0.54 \times 10^{-3}$	$0.97 \times 10^{-2}$	$0.96 \times 10^{-2}$
43	73.9652	-27.8216	0.2329	6.2334	$0.31 \times 10^{-2}$	$0.26 \times 10^{-3}$	$0.18 \times 10^{-1}$	$0.96 \times 10^{-2}$
44	77.9099	-26.6467	0.1470	7.2926	$0.22 \times 10^{-2}$	$0.30 \times 10^{-3}$	$0.12 \times 10^{-1}$	$0.10 \times 10^{-1}$
45	80.3824	-33.2035	0.1072	7.8795	$0.22 \times 10^{-2}$	$0.35 \times 10^{-3}$	$-0.39 \times 10^{-2}$	$0.97 \times 10^{-2}$
46	80.9954	-50.9072	0.2998	4.5969	$0.15 \times 10^{-2}$	$0.25 \times 10^{-3}$	$0.13 \times 10^{-1}$	$0.89 \times 10^{-2}$
47	83.2875	-31.0322	0.4120	3.9787	$0.12 \times 10^{-2}$	$0.22 \times 10^{-3}$	$-0.10 \times 10^{-1}$	$0.87 \times 10^{-2}$
48	85.9999	26.7107	0.1790	11.3240	$0.24 \times 10^{-2}$	$0.10 \times 10^{-2}$	$0.12 \times 10^{-1}$	$0.12 \times 10^{-1}$
49	86.4555	15.2999	0.2600	4.9172	$0.17 \times 10^{-2}$	$0.15 \times 10^{-3}$	$0.41 \times 10^{-3}$	$0.91 \times 10^{-2}$
50	92.7308	73.4614	0.2279	5.5586	$0.25 \times 10^{-2}$	$0.25 \times 10^{-3}$	$0.14 \times 10^{-1}$	$0.90 \times 10^{-2}$
51	93.9197	34.9077	0.0809	11.6216	$0.57 \times 10^{-2}$	$0.34 \times 10^{-3}$	$0.91 \times 10^{-2}$	$0.13 \times 10^{-1}$
52	94.0187	27.4256	0.2990	8.0500	$0.16 \times 10^{-2}$	$0.80 \times 10^{-3}$	$0.10 \times 10^{-1}$	$0.10 \times 10^{-1}$
53	96.8523	52.4668	0.3179	4.1455	$0.81 \times 10^{-3}$	$0.14 \times 10^{-3}$	$0.11 \times 10^{-2}$	$0.83 \times 10^{-2}$
54	97.7396	38.1199	0.1709	6.3915	$0.24 \times 10^{-2}$	$0.17 \times 10^{-3}$	$0.13 \times 10^{-1}$	$0.96 \times 10^{-2}$
55	98.9502	24.8610	0.0928	8.2040	$0.12 \times 10^{-2}$	$0.23 \times 10^{-3}$	$0.95 \times 10^{-3}$	$0.11 \times 10^{-1}$
56	106.7311	-83.2257	0.2924	4.2902	$0.20 \times 10^{-2}$	$0.24 \times 10^{-3}$	$0.11 \times 10^{-1}$	$0.83 \times 10^{-2}$
57	107.1124	65.3142	0.2799	4.9453	$0.17 \times 10^{-2}$	$0.20 \times 10^{-3}$	$0.21 \times 10^{-1}$	$0.88 \times 10^{-2}$
58	110.9809	31.7338	0.0581	16.6276	$0.13 \times 10^{-1}$	$0.50 \times 10^{-3}$	$0.14 \times 10^{-1}$	$0.14 \times 10^{-1}$
59	112.4561	57.0378	0.0701	11.2395	$0.29 \times 10^{-2}$	$0.35 \times 10^{-3}$	$0.15 \times 10^{-1}$	$0.13 \times 10^{-1}$
60	113.8229	44.3503	0.2250	4.6399	$0.65 \times 10^{-3}$	$0.13 \times 10^{-3}$	$0.65 \times 10^{-2}$	$0.87 \times 10^{-2}$

TABLE 2  
WMAP OBSERVATIONS OF *Planck* ESZ CLUSTERS

Index	Gal lon ( <i>l</i> ) (deg)	Gal lat ( <i>b</i> ) (deg)	Redshift	$\theta_{500}$ (arcmin)	$Y_{500}^{\text{planck}}$ (arcmin <sup>2</sup> )	$\delta Y_{500}^{\text{planck}}$ (arcmin <sup>2</sup> )	$Y_{500}^{\text{wmap}}$ (arcmin <sup>2</sup> )	$\delta Y_{500}^{\text{wmap}}$ (arcmin <sup>2</sup> )
61	114.3368	64.8740	0.2836	4.1782	$0.11 \times 10^{-2}$	$0.18 \times 10^{-3}$	$0.11 \times 10^{-1}$	$0.85 \times 10^{-2}$
62	115.1624	-72.0911	0.0555	18.8448	$0.12 \times 10^{-1}$	$0.99 \times 10^{-3}$	$0.12 \times 10^{-1}$	$0.15 \times 10^{-1}$
63	118.4482	39.3351	0.3967	3.4480	$0.86 \times 10^{-3}$	$0.14 \times 10^{-3}$	$0.58 \times 10^{-2}$	$0.74 \times 10^{-2}$
64	118.6016	28.5586	0.1780	5.9658	$0.12 \times 10^{-2}$	$0.25 \times 10^{-3}$	$0.15 \times 10^{-1}$	$0.96 \times 10^{-2}$
65	124.2179	-36.4859	0.1971	6.2310	$0.28 \times 10^{-2}$	$0.38 \times 10^{-3}$	$0.66 \times 10^{-2}$	$0.96 \times 10^{-2}$
66	125.5865	-64.1447	0.0442	17.7296	$0.78 \times 10^{-2}$	$0.92 \times 10^{-3}$	$0.18 \times 10^{-1}$	$0.14 \times 10^{-1}$
67	125.7057	53.8566	0.3019	4.1887	$0.10 \times 10^{-2}$	$0.15 \times 10^{-3}$	$-0.38 \times 10^{-2}$	$0.87 \times 10^{-2}$
68	139.1979	56.3560	0.3220	3.7032	$0.68 \times 10^{-3}$	$0.16 \times 10^{-3}$	$-0.65 \times 10^{-2}$	$0.79 \times 10^{-2}$
69	143.2459	65.2152	0.2110	4.8535	$0.12 \times 10^{-2}$	$0.19 \times 10^{-3}$	$0.10 \times 10^{-1}$	$0.90 \times 10^{-2}$
70	146.3311	-15.5913	0.0172	39.9005	$0.22 \times 10^{-1}$	$0.33 \times 10^{-2}$	$-0.28 \times 10^{-2}$	$0.21 \times 10^{-1}$
71	149.2421	54.1894	0.1369	7.3566	$0.29 \times 10^{-2}$	$0.26 \times 10^{-3}$	$0.10 \times 10^{-1}$	$0.97 \times 10^{-2}$
72	149.7332	34.6991	0.1818	6.9874	$0.33 \times 10^{-2}$	$0.30 \times 10^{-3}$	$0.78 \times 10^{-2}$	$0.93 \times 10^{-2}$
73	159.8592	-73.4730	0.2060	5.6338	$0.29 \times 10^{-2}$	$0.29 \times 10^{-3}$	$0.87 \times 10^{-2}$	$0.97 \times 10^{-2}$
74	161.4447	26.2337	0.0381	17.7570	$0.42 \times 10^{-2}$	$0.68 \times 10^{-3}$	$0.22 \times 10^{-1}$	$0.14 \times 10^{-1}$
75	163.7234	53.5331	0.1580	6.4145	$0.17 \times 10^{-2}$	$0.23 \times 10^{-3}$	$-0.30 \times 10^{-2}$	$0.98 \times 10^{-2}$
76	164.1859	-38.8932	0.0739	14.8848	$0.11 \times 10^{-1}$	$0.87 \times 10^{-3}$	$0.14 \times 10^{-1}$	$0.13 \times 10^{-1}$
77	165.0876	54.1196	0.1440	7.1812	$0.15 \times 10^{-2}$	$0.26 \times 10^{-3}$	$0.12 \times 10^{-1}$	$0.97 \times 10^{-2}$
78	166.1319	43.3926	0.2172	5.6392	$0.21 \times 10^{-2}$	$0.24 \times 10^{-3}$	$0.11 \times 10^{-1}$	$0.91 \times 10^{-2}$
79	167.6563	17.6484	0.1740	6.3019	$0.25 \times 10^{-2}$	$0.30 \times 10^{-3}$	$0.89 \times 10^{-3}$	$0.92 \times 10^{-2}$
80	171.9474	-40.6552	0.2700	5.9117	$0.34 \times 10^{-2}$	$0.32 \times 10^{-3}$	$0.15 \times 10^{-1}$	$0.94 \times 10^{-2}$
81	172.8864	65.3231	0.0794	9.4305	$0.16 \times 10^{-2}$	$0.33 \times 10^{-3}$	$0.23 \times 10^{-1}$	$0.11 \times 10^{-1}$
82	176.2823	-35.0506	0.0347	25.2705	$0.65 \times 10^{-2}$	$0.14 \times 10^{-2}$	$0.14 \times 10^{-1}$	$0.16 \times 10^{-1}$
83	180.2409	21.0459	0.5460	3.5482	$0.15 \times 10^{-2}$	$0.21 \times 10^{-3}$	$0.13 \times 10^{-1}$	$0.77 \times 10^{-2}$
84	180.6237	76.6529	0.2138	5.0805	$0.15 \times 10^{-2}$	$0.21 \times 10^{-3}$	$-0.91 \times 10^{-2}$	$0.94 \times 10^{-2}$
85	182.4440	-28.2986	0.0882	13.0626	$0.92 \times 10^{-2}$	$0.75 \times 10^{-3}$	$0.19 \times 10^{-1}$	$0.13 \times 10^{-1}$
86	182.6361	55.8245	0.2060	5.4790	$0.11 \times 10^{-2}$	$0.23 \times 10^{-3}$	$-0.38 \times 10^{-2}$	$0.91 \times 10^{-2}$
87	186.3949	37.2555	0.2820	5.0003	$0.28 \times 10^{-2}$	$0.25 \times 10^{-3}$	$0.53 \times 10^{-2}$	$0.86 \times 10^{-2}$
88	195.6242	44.0521	0.2952	3.8369	$0.92 \times 10^{-3}$	$0.19 \times 10^{-3}$	$0.11 \times 10^{-3}$	$0.80 \times 10^{-2}$
89	195.7735	-24.3063	0.2030	6.2071	$0.25 \times 10^{-2}$	$0.34 \times 10^{-3}$	$-0.55 \times 10^{-2}$	$0.92 \times 10^{-2}$
90	205.9614	-39.4838	0.4430	4.0854	$0.21 \times 10^{-2}$	$0.23 \times 10^{-3}$	$0.25 \times 10^{-1}$	$0.85 \times 10^{-2}$
91	209.5639	-36.4936	0.0326	25.2364	$0.90 \times 10^{-2}$	$0.12 \times 10^{-2}$	$-0.29 \times 10^{-1}$	$0.15 \times 10^{-1}$
92	216.6243	47.0225	0.3826	3.9972	$0.12 \times 10^{-2}$	$0.20 \times 10^{-3}$	$0.59 \times 10^{-2}$	$0.83 \times 10^{-2}$
93	218.8563	35.5065	0.1751	6.3049	$0.15 \times 10^{-2}$	$0.28 \times 10^{-3}$	$0.13 \times 10^{-1}$	$0.94 \times 10^{-2}$
94	226.1795	-21.9123	0.0989	9.1053	$0.26 \times 10^{-2}$	$0.39 \times 10^{-3}$	$0.55 \times 10^{-2}$	$0.11 \times 10^{-1}$
95	226.2475	76.7657	0.1427	7.9934	$0.32 \times 10^{-2}$	$0.35 \times 10^{-3}$	$0.19 \times 10^{-1}$	$0.10 \times 10^{-1}$
96	228.1552	75.1923	0.5450	3.1858	$0.88 \times 10^{-3}$	$0.18 \times 10^{-3}$	$0.29 \times 10^{-2}$	$0.78 \times 10^{-2}$
97	228.4974	53.1289	0.1434	6.7173	$0.12 \times 10^{-2}$	$0.28 \times 10^{-3}$	$-0.20 \times 10^{-1}$	$0.96 \times 10^{-2}$
98	229.2177	-17.2471	0.1710	5.6620	$0.17 \times 10^{-2}$	$0.26 \times 10^{-3}$	$0.87 \times 10^{-2}$	$0.93 \times 10^{-2}$
99	229.6413	77.9642	0.2690	4.2806	$0.15 \times 10^{-2}$	$0.23 \times 10^{-3}$	$-0.54 \times 10^{-2}$	$0.83 \times 10^{-2}$
100	229.9437	15.2954	0.0704	13.4113	$0.64 \times 10^{-2}$	$0.58 \times 10^{-3}$	$0.22 \times 10^{-1}$	$0.13 \times 10^{-1}$
101	234.5921	73.0189	0.0214	33.9178	$0.81 \times 10^{-2}$	$0.16 \times 10^{-2}$	$0.97 \times 10^{-2}$	$0.19 \times 10^{-1}$
102	236.9552	-26.6707	0.1483	7.1602	$0.17 \times 10^{-2}$	$0.29 \times 10^{-3}$	$0.83 \times 10^{-2}$	$0.10 \times 10^{-1}$
103	239.2841	24.7690	0.0542	18.1124	$0.18 \times 10^{-1}$	$0.68 \times 10^{-3}$	$0.11 \times 10^{-1}$	$0.15 \times 10^{-1}$
104	239.2893	-25.9962	0.4070	3.4432	$0.14 \times 10^{-2}$	$0.32 \times 10^{-3}$	$0.46 \times 10^{-2}$	$0.74 \times 10^{-2}$
105	241.7429	-30.8853	0.2708	4.4853	$0.16 \times 10^{-2}$	$0.20 \times 10^{-3}$	$0.65 \times 10^{-2}$	$0.85 \times 10^{-2}$
106	241.7782	-24.0010	0.1392	7.5582	$0.21 \times 10^{-2}$	$0.28 \times 10^{-3}$	$0.22 \times 10^{-1}$	$0.10 \times 10^{-1}$
107	241.8563	51.5311	0.0700	9.7408	$0.13 \times 10^{-2}$	$0.37 \times 10^{-3}$	$-0.12 \times 10^{-1}$	$0.12 \times 10^{-1}$
108	241.9745	14.8562	0.1687	6.2748	$0.23 \times 10^{-2}$	$0.26 \times 10^{-3}$	$0.13 \times 10^{-1}$	$0.94 \times 10^{-2}$
109	243.5701	67.7603	0.0834	10.4394	$0.34 \times 10^{-2}$	$0.40 \times 10^{-3}$	$0.61 \times 10^{-2}$	$0.12 \times 10^{-1}$
110	244.3430	-32.1379	0.2839	4.9752	$0.16 \times 10^{-2}$	$0.21 \times 10^{-3}$	$0.22 \times 10^{-2}$	$0.87 \times 10^{-2}$
111	244.6968	32.4925	0.1535	6.2505	$0.16 \times 10^{-2}$	$0.25 \times 10^{-3}$	$-0.32 \times 10^{-2}$	$0.93 \times 10^{-2}$
112	246.5206	-26.0574	0.0468	15.4600	$0.29 \times 10^{-2}$	$0.54 \times 10^{-3}$	$0.19 \times 10^{-1}$	$0.14 \times 10^{-1}$
113	247.1750	-23.3277	0.1520	6.3719	$0.11 \times 10^{-2}$	$0.23 \times 10^{-3}$	$-0.37 \times 10^{-2}$	$0.11 \times 10^{-1}$
114	249.8766	-39.8654	0.1501	6.2807	$0.10 \times 10^{-2}$	$0.22 \times 10^{-3}$	$-0.58 \times 10^{-2}$	$0.96 \times 10^{-2}$
115	250.9065	-36.2550	0.2000	5.5837	$0.16 \times 10^{-2}$	$0.21 \times 10^{-3}$	$0.10 \times 10^{-1}$	$0.92 \times 10^{-2}$
116	252.9668	-56.0549	0.0752	13.1950	$0.26 \times 10^{-2}$	$0.39 \times 10^{-3}$	$0.71 \times 10^{-2}$	$0.13 \times 10^{-1}$
117	253.4796	-33.7242	0.1913	5.3897	$0.12 \times 10^{-2}$	$0.19 \times 10^{-3}$	$-0.13 \times 10^{-1}$	$0.94 \times 10^{-2}$
118	256.4510	-65.7122	0.2195	5.3944	$0.16 \times 10^{-2}$	$0.22 \times 10^{-3}$	$0.33 \times 10^{-2}$	$0.94 \times 10^{-2}$
119	257.3436	-22.1833	0.2026	5.1414	$0.11 \times 10^{-2}$	$0.16 \times 10^{-3}$	$-0.24 \times 10^{-2}$	$0.88 \times 10^{-2}$
120	260.0328	-63.4448	0.2836	4.6171	$0.13 \times 10^{-2}$	$0.19 \times 10^{-3}$	$0.43 \times 10^{-2}$	$0.87 \times 10^{-2}$

TABLE 2  
WMAP OBSERVATIONS OF *Planck* ESZ CLUSTERS

Index	Gal lon ( <i>l</i> ) (deg)	Gal lat ( <i>b</i> ) (deg)	Redshift	$\theta_{500}$ (arcmin)	$Y_{500}^{\text{planck}}$ (arcmin <sup>2</sup> )	$\delta Y_{500}^{\text{planck}}$ (arcmin <sup>2</sup> )	$Y_{500}^{\text{wmap}}$ (arcmin <sup>2</sup> )	$\delta Y_{500}^{\text{wmap}}$ (arcmin <sup>2</sup> )
121	262.2535	-35.3691	0.2952	4.8608	$0.19 \times 10^{-2}$	$0.14 \times 10^{-3}$	$0.46 \times 10^{-2}$	$0.88 \times 10^{-2}$
122	262.7108	-40.9137	0.3900	3.7414	$0.11 \times 10^{-2}$	$0.13 \times 10^{-3}$	$-0.31 \times 10^{-2}$	$0.79 \times 10^{-2}$
123	263.1612	-23.4141	0.2266	5.7940	$0.18 \times 10^{-2}$	$0.18 \times 10^{-3}$	$0.27 \times 10^{-2}$	$0.93 \times 10^{-2}$
124	263.2091	-25.2105	0.0506	15.3956	$0.41 \times 10^{-2}$	$0.48 \times 10^{-3}$	$0.15 \times 10^{-1}$	$0.14 \times 10^{-1}$
125	263.6653	-22.5362	0.1644	7.1784	$0.36 \times 10^{-2}$	$0.22 \times 10^{-3}$	$0.51 \times 10^{-2}$	$0.99 \times 10^{-2}$
126	265.0068	-48.9483	0.0590	15.5042	$0.65 \times 10^{-2}$	$0.53 \times 10^{-3}$	$0.15 \times 10^{-3}$	$0.13 \times 10^{-1}$
127	266.0384	-21.2523	0.2965	5.3920	$0.37 \times 10^{-2}$	$0.18 \times 10^{-3}$	$0.11 \times 10^{-1}$	$0.92 \times 10^{-2}$
128	266.8423	25.0788	0.2542	5.4913	$0.15 \times 10^{-2}$	$0.23 \times 10^{-3}$	$0.27 \times 10^{-2}$	$0.90 \times 10^{-2}$
129	269.3112	-49.8784	0.0853	9.4591	$0.22 \times 10^{-2}$	$0.36 \times 10^{-3}$	$-0.98 \times 10^{-2}$	$0.12 \times 10^{-1}$
130	269.5163	26.4247	0.0126	43.3013	$0.12 \times 10^{-1}$	$0.16 \times 10^{-2}$	$-0.39 \times 10^{-2}$	$0.22 \times 10^{-1}$
131	271.1969	-30.9695	0.3700	4.0128	$0.11 \times 10^{-2}$	$0.12 \times 10^{-3}$	$0.10 \times 10^{-2}$	$0.80 \times 10^{-2}$
132	271.5017	-56.5590	0.3000	4.0513	$0.14 \times 10^{-2}$	$0.39 \times 10^{-3}$	$-0.35 \times 10^{-2}$	$0.82 \times 10^{-2}$
133	272.1077	-40.1502	0.0589	16.8371	$0.16 \times 10^{-1}$	$0.65 \times 10^{-3}$	$0.10 \times 10^{-1}$	$0.14 \times 10^{-1}$
134	273.6439	63.2815	0.1339	7.5915	$0.28 \times 10^{-2}$	$0.40 \times 10^{-3}$	$0.88 \times 10^{-2}$	$0.10 \times 10^{-1}$
135	275.2199	43.9212	0.1068	8.6906	$0.24 \times 10^{-2}$	$0.46 \times 10^{-3}$	$0.22 \times 10^{-1}$	$0.11 \times 10^{-1}$
136	277.7522	-51.7307	0.4400	3.5019	$0.15 \times 10^{-2}$	$0.18 \times 10^{-3}$	$0.14 \times 10^{-1}$	$0.77 \times 10^{-2}$
137	278.6061	39.1716	0.3075	4.6768	$0.19 \times 10^{-2}$	$0.30 \times 10^{-3}$	$0.13 \times 10^{-1}$	$0.86 \times 10^{-2}$
138	280.1968	47.8167	0.1557	6.1951	$0.23 \times 10^{-2}$	$0.34 \times 10^{-3}$	$-0.17 \times 10^{-4}$	$0.99 \times 10^{-2}$
139	282.4933	65.1743	0.0766	12.0485	$0.53 \times 10^{-2}$	$0.69 \times 10^{-3}$	$0.34 \times 10^{-1}$	$0.13 \times 10^{-1}$
140	284.4608	52.4371	0.4414	3.6666	$0.16 \times 10^{-2}$	$0.25 \times 10^{-3}$	$0.47 \times 10^{-2}$	$0.78 \times 10^{-2}$
141	284.9936	-23.7081	0.3900	3.9007	$0.13 \times 10^{-2}$	$0.12 \times 10^{-3}$	$0.89 \times 10^{-2}$	$0.81 \times 10^{-2}$
142	285.6352	-17.2466	0.3500	3.5369	$0.90 \times 10^{-3}$	$0.15 \times 10^{-3}$	$0.53 \times 10^{-2}$	$0.77 \times 10^{-2}$
143	286.5869	-31.2510	0.2100	5.6231	$0.14 \times 10^{-2}$	$0.21 \times 10^{-3}$	$-0.34 \times 10^{-2}$	$0.91 \times 10^{-2}$
144	286.9927	32.9157	0.3900	5.0661	$0.34 \times 10^{-2}$	$0.33 \times 10^{-3}$	$0.20 \times 10^{-1}$	$0.91 \times 10^{-2}$
145	288.6160	-37.6562	0.1270	7.1712	$0.29 \times 10^{-2}$	$0.31 \times 10^{-3}$	$0.90 \times 10^{-3}$	$0.98 \times 10^{-2}$
146	292.5194	21.9886	0.3000	5.1319	$0.21 \times 10^{-2}$	$0.34 \times 10^{-3}$	$0.18 \times 10^{-1}$	$0.91 \times 10^{-2}$
147	294.6674	-37.0299	0.2742	4.4588	$0.15 \times 10^{-2}$	$0.20 \times 10^{-3}$	$0.68 \times 10^{-2}$	$0.84 \times 10^{-2}$
148	295.3328	23.3359	0.1190	7.2625	$0.23 \times 10^{-2}$	$0.43 \times 10^{-3}$	$0.15 \times 10^{-2}$	$0.10 \times 10^{-1}$
149	296.4139	-32.4851	0.0613	12.4130	$0.25 \times 10^{-2}$	$0.40 \times 10^{-3}$	$0.19 \times 10^{-1}$	$0.13 \times 10^{-1}$
150	303.7589	33.6561	0.0544	13.6334	$0.47 \times 10^{-2}$	$0.80 \times 10^{-3}$	$0.14 \times 10^{-1}$	$0.13 \times 10^{-1}$
151	304.4970	32.4428	0.0554	13.9820	$0.37 \times 10^{-2}$	$0.82 \times 10^{-3}$	$0.49 \times 10^{-2}$	$0.13 \times 10^{-1}$
152	304.6716	-31.6688	0.1934	5.1350	$0.11 \times 10^{-2}$	$0.20 \times 10^{-3}$	$-0.14 \times 10^{-2}$	$0.89 \times 10^{-2}$
153	304.8952	45.4509	0.0473	17.6562	$0.84 \times 10^{-2}$	$0.10 \times 10^{-2}$	$-0.25 \times 10^{-1}$	$0.14 \times 10^{-1}$
154	306.6839	61.0626	0.0845	11.5603	$0.52 \times 10^{-2}$	$0.65 \times 10^{-3}$	$-0.15 \times 10^{-2}$	$0.12 \times 10^{-1}$
155	306.8008	58.6075	0.0845	11.8327	$0.43 \times 10^{-2}$	$0.68 \times 10^{-3}$	$-0.43 \times 10^{-2}$	$0.13 \times 10^{-1}$
156	311.9973	30.7170	0.0480	19.4676	$0.12 \times 10^{-1}$	$0.13 \times 10^{-2}$	$0.15 \times 10^{-1}$	$0.14 \times 10^{-1}$
157	313.3604	61.1166	0.1832	7.4682	$0.39 \times 10^{-2}$	$0.44 \times 10^{-3}$	$0.78 \times 10^{-2}$	$0.95 \times 10^{-2}$
158	313.8723	-17.1066	0.1530	8.1257	$0.43 \times 10^{-2}$	$0.38 \times 10^{-3}$	$0.16 \times 10^{-1}$	$0.11 \times 10^{-1}$
159	315.7076	-18.0430	0.1050	9.6202	$0.49 \times 10^{-2}$	$0.46 \times 10^{-3}$	$0.16 \times 10^{-1}$	$0.11 \times 10^{-1}$
160	316.3467	28.5433	0.0391	24.8271	$0.21 \times 10^{-1}$	$0.17 \times 10^{-2}$	$0.17 \times 10^{-1}$	$0.16 \times 10^{-1}$
161	318.1334	-29.5778	0.2170	5.1100	$0.17 \times 10^{-2}$	$0.26 \times 10^{-3}$	$0.31 \times 10^{-2}$	$0.86 \times 10^{-2}$
162	321.9628	-47.9754	0.0940	9.9841	$0.29 \times 10^{-2}$	$0.32 \times 10^{-3}$	$0.13 \times 10^{-1}$	$0.12 \times 10^{-1}$
163	324.4983	-44.9709	0.0951	8.9942	$0.21 \times 10^{-2}$	$0.30 \times 10^{-3}$	$-0.13 \times 10^{-1}$	$0.11 \times 10^{-1}$
164	332.2345	-46.3695	0.0980	10.4829	$0.47 \times 10^{-2}$	$0.38 \times 10^{-3}$	$0.18 \times 10^{-2}$	$0.12 \times 10^{-1}$
165	332.8879	-19.2803	0.1470	7.1985	$0.24 \times 10^{-2}$	$0.32 \times 10^{-3}$	$0.59 \times 10^{-2}$	$0.97 \times 10^{-2}$
166	335.5923	-46.4637	0.0760	11.4352	$0.46 \times 10^{-2}$	$0.42 \times 10^{-3}$	$0.19 \times 10^{-1}$	$0.13 \times 10^{-1}$
167	336.5914	-55.4487	0.0965	9.5308	$0.32 \times 10^{-2}$	$0.32 \times 10^{-3}$	$0.12 \times 10^{-1}$	$0.12 \times 10^{-1}$
168	340.8860	-33.3489	0.0556	18.6213	$0.15 \times 10^{-1}$	$0.78 \times 10^{-3}$	$0.18 \times 10^{-1}$	$0.15 \times 10^{-1}$
169	340.9585	35.1160	0.2357	6.0862	$0.17 \times 10^{-2}$	$0.38 \times 10^{-3}$	$-0.14 \times 10^{-1}$	$0.98 \times 10^{-2}$
170	342.3172	-34.9065	0.2320	4.8257	$0.16 \times 10^{-2}$	$0.24 \times 10^{-3}$	$-0.41 \times 10^{-2}$	$0.91 \times 10^{-2}$
171	342.8155	-30.4605	0.0600	10.9597	$0.24 \times 10^{-2}$	$0.51 \times 10^{-3}$	$0.39 \times 10^{-1}$	$0.13 \times 10^{-1}$
172	345.4068	-39.3440	0.0448	23.7182	$0.60 \times 10^{-2}$	$0.18 \times 10^{-2}$	$-0.16 \times 10^{-1}$	$0.15 \times 10^{-1}$
173	346.5981	35.0477	0.2226	5.3936	$0.26 \times 10^{-2}$	$0.31 \times 10^{-3}$	$0.31 \times 10^{-3}$	$0.89 \times 10^{-2}$
174	347.1876	-27.3538	0.2371	4.9553	$0.12 \times 10^{-2}$	$0.24 \times 10^{-3}$	$0.25 \times 10^{-2}$	$0.93 \times 10^{-2}$
175	349.4626	-59.9475	0.3475	4.9888	$0.25 \times 10^{-2}$	$0.19 \times 10^{-3}$	$0.15 \times 10^{-1}$	$0.92 \times 10^{-2}$

- Birkinshaw M., & Gull S. F., 1978, *Nature*, 274, 111  
Birkinshaw M., 1999, *Phys. Rep.*, 310, 97  
Carlstrom J. E., Holder G. P., & Reese E. D., 2002, *ARA&A*, 40, 643  
Carlstrom J. E., 2011, *Publ. Astron. Soc. Pac.* 123, 568-581  
Clutton-Brock M., 1967, *Technometrics*, 9, 261  
Douspis M., Aghanim N., & Langer M., 2006, *A&A*, 456, 819  
Gorski K. M., Hivon E., Banday A. J., Wandelt B. D., Hansen F. K., Reinecke M., & Bartelmann M., 2005, *ApJ* 622, 759  
Haiman Z., Mohr J. J., & Holder G. P., 2001, *ApJ*, 553, 545  
Hinshaw G. et al., 2007, *ApJS*, 170, 288  
Komatsu E., 2011, *ApJS*, 192, 18  
WMAP Lambda website: <http://lambda.gsfc.nasa.gov/>  
Levine E. S., Schulz A. E., & White M., 2002, *ApJ*, 577, 569  
Majumdar S., & Mohr J. J., 2004, *ApJ*, 613, 41  
Marriage T. A., 2011, *ApJ*, 737, 61  
Melin J., Bartlett J. G., Delabrouille J., 2006, *A&A*, 459, 341  
McCarthy I. G., Bower R. G., Balogh M. L., 2007, *MNRAS*, 377, 1457-1463  
Nagai D., Kravtsov A. V., & Vikhlinin A., 2007, *ApJ*, 668, 1  
The Planck Collaboration, *Planck: The Scientific Programme*, European Space Agency Vol. No. ESA/CSCI (2005)1, edited by G. Efstathiou, et al. (ESA Publications, Noordwijk, Netherlands, 2005).  
Planck Collaboration VII, 2011, *A&A*, 536, 7  
Planck Collaboration VIII, 2011, *A&A*, 536, 8  
Planck Collaboration IX, 2011, *A&A*, 536, 9  
Planck Collaboration XII, 2011, *A&A*, 536, 12  
Press W. H., Teukolsky S. A., Vetterling W. T., & Flannery B. P., *Numerical Recipes* 3rd edition, 2007, Cambridge University Press.  
Tegmark M. & Efstathiou G., 1996, *MNRAS*, 281, 1297  
Tegmark M. & de Oliveira-Costa A., 1998, *ApJ*, 500, 83  
Shaw L. D., Rudd D. H., & Nagai D., 2012, *ApJ*, 756, 15  
Sunyaev R. A., & Zeldovich Y. B., 1972, *Comments on Astrophysics and Space Physics*, 4, 173  
Sunyaev R. A., & Zeldovich I. B., 1980, *ARA&A*, 18, 537  
Weller J., Battye R. A., & Kneissl R., 2002, *Phys. Rev. Lett.*, 88, 231301  
Whitbourn J. R., Shanks T., & Sawangwit U., arXiv:1107.2654 [astro-ph].  
Zwart J. T. L. et al., 2008, *MNRAS*, 391, 1545